Comparison of a Spectral Bin and Two Multi-Moment Bulk Microphysics Schemes for Supercell Simulation: Investigation into Key Processes Responsible for Hydrometeor Distributions and Precipitation

Marcus Johnson[1,2], Ming Xue[1,2,*], and Youngsun Jung[1,2,†]

[1]Center for Analysis and Prediction of Storms and

[2]School of Meteorology, University of Oklahoma, Norman, OK 73072, USA,

Submitted to Advances in Atmospheric Sciences

March 2023

Revised July 2023

Revised September 2023

*Corresponding author: Ming Xue (mxue@ou.edu)

†Current Affiliation: Office of Science and Technology Integration, National Weather Service, Silver Spring, MD 20910, USA

Abstract

There are more uncertainties with ice hydrometeor representations and related processes than liquid hydrometeors within microphysics parameterization (MP) schemes because of their complicated geometries and physical properties. Idealized supercell simulations are produced using the WRF model coupled with “full” Hebrew University spectral bin MP (HU-SBM), and NSSL and Thompson bulk MP (BMP) schemes. HU-SBM downdrafts are typically weaker than those of the NSSL and Thompson simulations, accompanied by less rain evaporation. HU-SBM produces more cloud ice (plates), graupel, and hail than the BMPs yet precipitates less at the surface. The limiting mass bins (and subsequently, particle size) of rimed ice in HU-SBM and slower rimed ice fall speeds lead to smaller melting-level net rimed ice fluxes than those of the BMPs. Aggregation from plates in HU-SBM, together with snow-graupel collisions, leads to a greater snow contribution to rain than those of the BMPs. Replacing HU-SBM’s fall speeds using the formulations of the BMPs after aggregating the discrete bin values to mass mixing ratios and total number concentrations increases net rain and rimed ice fluxes. Still, they are smaller in magnitude than bulk rain, NSSL hail, and Thompson graupel net fluxes near the surface. Conversely, the melting-layer net rimed ice fluxes are reduced when the fall speeds for the NSSL and Thompson simulations are calculated using HU-SBM fall speed formulations after discretizing the bulk particle size distributions (PSDs) into spectral bins. The results highlight precipitation sensitivity to storm dynamics, fall speed, hydrometeor evolution governed by process rates, and MP PSD design.

Key words: Precipitation, spectral bin microphysics, bulk microphysics parameterization, microphysics processes, WRF model, supercell storm https://doi.org/10.1007/s00376-023-3069-7

Article highlights:

- HU-SBM “full” version simulates less precipitation than the bulk NSSL and Thompson schemes
- Rain mass sourced from snow in HU-SBM is larger than those in the BMPs, partly due to large plate production and subsequent aggregation
- Limiting maximum mass bins and generally slower rimed ice fall speeds than those of the BMPs lower rimed ice flux in HU-SBM

1. Introduction

Microphysics parameterization (MP) uncertainty remains a substantial source of numerical weather prediction (NWP) model error. One to two hydrometeor categories, demarcated by smaller cloud droplets and larger rain drops, can simulate spherical liquid particles with water density without much error. In contrast, parameterizations of ice particles in MP schemes continue to lag in sophistication relative to the complex geometrical spectra of observed ice habits. While ice crystal diagrams have documented observed habits for a given ambient temperature and ice supersaturation, the oscillatory nature of plates and columns with changes in temperature (as well as often-observed asymmetrical crystals and complex polycrystal structure; Bailey and Hallett, 2009) preclude an exact, quantitative relationship linking ice crystal geometry to the ambient thermodynamic state. Aggregates of crystals may also form additional habits, with even more distinct habits if these ice particles rime (e.g., Magono and Lee, 1966; Heymsfield and Kajikawa, 1987; Pruppacher and Klett, 1997). Therefore, ice habits are inevitably oversimplified in NWP models as it is impossible to parameterize every observed ice type with a few ice hydrometeor categories, such as the typically used cloud ice, snow/aggregates, graupel and/or hail.

The evolution of the particle size distribution (PSD) of a hydrometeor category in NWP models is typically modelled in either a bulk or spectral bin framework. Bulk MP parameterization schemes (BMPs) assume certain forms of hydrometeor PSDs containing a few free parameters (e.g., Lin et al., 1983; Ulbrich, 1983; Chen and Sun, 2002) while spectral bin MP schemes (SBMs) discretize the PSDs into spectral bins, generally predicting the evolution of either the PSDs themselves or moments in each bin (e.g., Hall, 1980; Reisin et al., 1996; Geresdi, 1998). SBMs' discrete PSD bins allow the parameterization of particle attributes (e.g., axis ratio, density) with greater flexibility and precision than BMPs across the hydrometeor spectra, albeit at potentially higher computational costs. For more details, readers are referred to a comprehensive review of bulk and spectral bin schemes by Khain et al. (2015).

Despite many complex observed geometric modes of ice particles, MP schemes attempt to represent the ice spectra across a limited number of ice categories (e.g., cloud ice, snow, graupel, hail; Geresdi, 1998; Milbrandt and Yau, 2005a, b). BMPs include spherical (e.g., Ferrier, 1994; Morrison et al., 2009) and non-spherical crystal/snow (e.g., Cox, 1988; Hong et al., 2004) more consistent with observations (e.g., Mitchell et al., 1990). BMPs may contain constant (e.g., Ferrier 1994) or predicted rimed ice density (e.g., Mansell et al., 2010). Further, the Predicted Particle Properties (P3; Morrison and Milbrandt, 2015; Milbrandt et al., 2021) and Ice-Spheroid Habit Model with Aspect-Ratio Evolution (ISHMAEL; Jensen et al., 2017) BMPs remove distinct ice categories in favor of free-evolving ice particles in each category (although ISHMAEL contains a separate aggregate category for ice property preservation), reducing ad-hoc simulated ice conversions.

SBM PSD discretization allows for greater precision of ice particle and process parameterization compared to BMPs. Young (1974) and Takahashi (1976) partitioned ice crystal size bins into *x*- and *z*- dimensions, while separate ice crystal habits as hydrometeor categories (e.g., columns, dendrites) were also added to some SBMs (Khain and Sednev, 1996; Khain et al., 2004). The expansion from 33 to 43 bins within the Hebrew University Cloud Model (HUCM) SBM “full” version and improved graupel to hail conversion facilitated large rimed ice particles and reflectivities as simulated by a polarimetric radar simulator in deep convection (Ryzhkov et al., 2011). Still, increasing ice complexity using SBM hydrometeor representation does not always guarantee more accurate simulations relative to BMPs (e.g., Fan et al., 2017; Xue et al., 2017) because of a large number of uncertainties with the MP processes involved. While these papers and others (e.g., Kumjian et al., 2014; Shpund et al., 2019) demonstrate reasonable ability of SBMs to simulate deep convection, SBMs (and BMPs) require detailed assessment and understanding of hydrometeor evolution when applied to different types of convective storms.

Supercell microphysical processes are typically dominated by rain and rimed ice given the storm’s deep convective updraft (e.g., Kumjian and Ryzhkov, 2008). Simulated cloud water, cloud ice, and snow provide pathways to rain and rimed ice creation and growth (see Figure 4 in Morrison et al., 2020), highlighting their potential roles in particle evolution within supercell thunderstorms. Further, the limited three-dimensional idealized supercell simulation studies that exist using the Weather Research and Forecasting (WRF; Skamarock et al., 2008) model coupled with HUCM “full” microphysics (HU-SBM; Khain and Lynn, 2009; Heikenfeld et al., 2019) have mainly focused on model sensitivities (e.g., aerosol concentration) related to, rather than in-depth evaluations of, microphysical processes controlling SBM hydrometeor evolutions. In this study, we examine hydrometeor evolutions in idealized supercell simulations using the HU-SBM and two-moment NSSL and Thompson BMP schemes within the community WRF model. We investigate their underlying representations and MP processes primarily responsible for significant differences found in the simulations. Such a study can help clarify how each MP scheme simulates complex ice spectra and their impact on the liquid spectra, and provide guidance on improving the schemes’ representation and evolution of ice with a limited number of hydrometeor categories. Insights gained from analyzing idealized simulations can help guide future SBM/BMP improvement when applied to real cases by establishing a link between MP treatments and the expected results of storm simulation.

The rest of this paper is organized as follows: section 2 details the simulation model setup, section 3 compares simulated precipitation and hydrometeor profiles to analyze hydrometeor behavior (e.g., potential relative biases) within the storm. Section 4 investigates hydrometeor vertical flux profiles and their link to surface precipitation, and section 5 summarizes and further discusses dynamic and microphysical effects on precipitation in the spectral and bulk frameworks examined in this paper.

2. Simulation experiment design

2.1 Numerical model

Idealized simulations of supercell thunderstorms are performed using the compressible, nonhydrostatic WRF model version 3.7.1 (Skamarock et al., 2008). Model configuration is detailed in Table 1 and is similar to the idealized supercell simulations in Johnson et al. (2016) and Johnson et al. (2019). Storms are simulated for 2 h on a 200 km x 200 km grid with a 1 km horizontal spacing. The vertical grid extends to 20 km height with an approximate 500 m grid spacing. The Weisman and Klemp (1982) thermodynamic sounding with a veering quarter-circle wind profile (clockwise shear of 5.23×10^{-3} s^{-1} up to 2.3 km, unidirectional shear of 5.69×10^{-3} s^{-1} above to 7 km) is employed for the atmospheric environment, resulting in a convective available potential energy (CAPE) of approximately 2163 J kg^{-1} and storm-relative helicity (SRH) in the 0-3 km layer of approximately 180 m^2 s^{-2}. The storm is initiated using an ellipsoidal thermal bubble with a maximum potential temperature perturbation of 3 K. Radiation, land surface, cumulus, and planetary boundary layer parameterizations are turned off.

2.2 Microphysics schemes

As mentioned earlier, three MP schemes with varying degrees of complexity in representing hydrometeors, as available in WRF v3.7.1, are used in the supercell simulations. They are, respectively, the HUCM "full" SBM (Khain and Sednev, 1996; Khain et al., 2004), the fully two-moment National Severe Storms Laboratory (NSSL; Mansell et al., 2010), and the partially two-moment Thompson (Thompson et al., 2008) BMP schemes.

The HU-SBM "full" scheme prognoses the PSDs of liquid (one category spanning all drop sizes), three ice crystals (plates, columns, dendrites), (snow) aggregates, graupel, and hail, which are discretized into 33 mass-doubling bins ranging from 3.35×10^{-11} to 1.44×10^{-1} g. There are no processes in the HU-SBM "full" scheme that convert ice crystal habit to other habits after nucleation (in which ice crystal destination is determined by ambient temperature). An alternative "fast" (in contrast to "full") version of HU-SBM available in WRF prognoses the PSDs of one liquid and fewer ice categories, including ice crystals/aggregates, and graupel/hail, that are discretized into 33 or 43 bins. Studies (e.g., Khain et al., 2016; Shpund et al., 2019) have shown that the HU-SBM "fast" version has skill simulating deep convection. In this study, we choose to evaluate the HU-SBM "full" version because of its inclusion of more ice categories (6 vs. 2) which we believe are important for supercell storms. The use of 33 bins with smaller maximum diameters than the available 43 bins in the "fast" version does impose some limitation; therefore, results related to the maximum bin sizes do not necessarily carry over to the "fast" version. Hereafter, HU-SBM with no qualifier refers to the "full" version.

The NSSL BMP prognoses mass mixing ratio q_x and total number concentration N_{tx} (x refers to species) of cloud water, rain, cloud ice, snow, graupel, and hail, and additionally particle volume of graupel and hail which can be used to predict bulk density. The Thompson scheme prognoses q_x of cloud water, rain, cloud ice, snow, and graupel, and N_{tx} of cloud ice and rain. Among many available BMPs, the NSSL scheme is one of the most sophisticated two-moment BMPs and has been shown to outperform other BMPs in supercell simulations (Johnson et al. 2016, 2019), while the Thompson scheme is employed in the U.S. operational High-Resolution

Rapid Refresh forecasting system (HRRR; Benjamin et al., 2016) and has generally good performance for precipitation forecast.

We would like to point out that hydrometeors in each MP scheme may contain different assumptions of PSDs and particle properties. Liquid, plates, graupel, and hail in the HU-SBM contain constant bulk densities of 1000, 900, 400, and 900 kg m^{-3}, respectively, across their discretized mass bins, while column, dendrite, and snow bulk densities decrease at larger mass. Rain, graupel and hail in the NSSL scheme assume gamma PSDs (e.g., Ulbrich, 1983) with shape parameters $\alpha = 0$, 0, and 1, respectively. Cloud water, cloud ice, and snow have mass-dependent (rather than the commonly utilized diameter-dependent) gamma distributions with shape parameters $\alpha = 0$, 0, and –0.8 (Zrnic et al., 1993) respectively. Cloud water, cloud ice, rain, and snow have bulk densities of 1000, 900, 1000, and 100 kg m^{-3} respectively. Graupel and hail bulk densities are predicted via their bulk prognosed volumes. The Thompson scheme assumes an exponential PSD (gamma PSD with shape parameter $\alpha = 0$) for cloud ice, rain, and graupel, and a gamma PSD ($\alpha = 12$) for cloud water. Snow in the scheme follows a linear combination of exponential and gamma PSDs (Field et al., 2005; Thompson et al., 2008). Cloud water, cloud ice, rain and graupel have bulk densities of 1000, 890, 1000 and 500 kg m^{-3}, respectively, while snow density decreases with increasing diameter (similar to HU-SBM snow).

3. Simulated hydrometeors and microphysical processes

The supercells simulated using the three schemes are first examined in terms of the simulated horizontal reflectivity Z_H through the updraft (Figure 1). Z_H is calculated using the Center for Analysis and Prediction of Storms Polarimetric Radar data Simulator (CAPS-PRS; e.g., Jung et al., 2008; Dawson et al., 2014; Johnson et al., 2016), which utilizes the T-matrix method (Waterman, 1969; Vivekanandan et al., 1991) to calculate scattering amplitudes as a function of particle diameter and water fraction. Particle diameter is calculated assuming a spherical shape using the mass bins of hydrometeors in the HU-SBM. q_x and N_{tx} in the 2M bulk schemes are utilized to diagnose hydrometeor PSDs, while water fraction is diagnosed following Jung et al. (2008). For the HU-SBM scheme, wet snow diameter is recalculated based on the mixed-phase hydrometeor's new density taking into account the shrinking of the horizontal dimension of snow with progressive melting as in Jung et al. (2008). Given the ice crystal complexity of the HU-SBM, ice crystals are now included in the simulator for the scheme and are assumed to melt when ambient temperature exceeds 0 °C. Columns, plates, and dendrites are assumed to have aspect ratios of observed solid columns ($L/d \leq 2$), solid thick plates, and dendrites, respectively (Matrosov et al., 1996). Oblate (i.e., plates and dendrites) crystal orientation is assumed to follow a two-dimensional axisymmetric Gaussian distribution with a mean canting angle of 0° and standard deviation of 10°, while prolates (i.e., columns) follow a blend of fully chaotic and horizontal random orientation (Ryzhkov et al., 2011). For other hydrometeor orientation assumptions, we refer the reader to Johnson et al. (2016).

The simulated storms with NSSL and Thompson BMPs have noticeably larger reflectivities than those of the HU-SBM through their updraft cores at a mature supercell stage (t = 100 min; Figures 1a,c,e), consistent with reflectivity calculated in the microphysics schemes using the Rayleigh approximation. As reflectivity in these simulations is primarily dictated by rain, graupel, and hail (as expected in a deep, convective storm), further hydrometeor analysis will help clarify which parameterizations/processes (e.g., wet growth, fall speed) are primily responsible for the low reflectivity when HU-SBM is employed compared to the two bulk schemes. We also note that HU-SBM's (snow) aggregate contribution to reflectivity is larger and more widespread near and below the melting level compared to those in simulations using the two bulk schemes. Because of their small sizes, the contribution of HU-SBM ice crystals to reflectivity is generally small. Differences are also seen in the cold pool structures of the MP storm simulations (Figures 1b,d,f). The cold pool intensity reflects downdraft intensity, water loading, and evaporative/melting cooling. Later analyses on the microphysical process rates will reveal differences in evaporative cooling among the simulations. The Thompson simulation, which has the strongest downdrafts, produces the strongest cold pool (Figure 1f). HU-SBM downdrafts are weaker than those in the NSSL simulation, leading to a much weaker cold pool (Figures 1b,d). Stronger downdrafts may influence precipitation by transporting more mass to lower levels in addition to hydrometeor sedimentation.

One striking difference between the three simulations differing in microphysics only is the large discrepancy of domain-averaged accumulated precipitation, with the NSSL and Thompson simulations producing similar precipitation amounts that are approximately 5 times that (~1.45-1.7 mm) of the HU-SBM simulation (~0.3 mm) by the end of the two-hour runs (Figure 2). We note here that precipitation in the HU-SBM simulation might be delayed, as its domain-averaged accumulated precipitation near t = 200 min is similar to those of the bulk simulations near t = 120 min. HU-SBM precipitation is still smaller than those of the two bulk simulations when extended to 5 h (not shown). We also note that the HU-SBM "fast" version with 43 bins simulates precipitation amounts similar to those in the NSSL and Thompson simulations; however, it is outside the scope of this paper to determine the causes of simulation differences between the "fast" and "full" versions. The comparatively low amount of precipitation simulated using the HUCM "full" MP has been previously noted in idealized supercell simulations. Khain and Lynn (2009) speculated that the much stronger updrafts (and possibly larger autoconversion rate) in the Thompson simulation compared to those in HU-SBM helped contribute to its larger amount of precipitation. Our HU-SBM simulation contains updraft speed that is comparable to those of the NSSL and Thompson simulations (Figure 1). Falk et al. (2019) noted the HUCM “full” MP simulated more precipitation when using faster snow, graupel, and hail bulk fall speeds applied to its bins, but still less than the amount produced by the bulk simulations. The influence of microphysics was not investigated further. Therefore, an investigation into rain and ice hydrometeor mass and related processes, and vertical hydrometoer fluxes, are needed to understand the key causes of the precipitation differences between the HU-SBM and bulk simulations.

3.1 Temporal evolution of hydrometeors

As MP-simulated hydrometeors directly contribute to the amount of available mass to sediment to the surface, it is logical to investigate the temporal evolution of each simulation’s domain-averaged mass (Figure 3). Figure 4 shows the time series of domain-averaged 5-min accumulated microphysics rates for different species. While there is no traditional cloud water category in HU-SBM because all liquid is contained in its liquid hydrometeor category, HU-SBM does output “cloud water” mass corresponding to liquid bins with a maximum diameter of 0.16 mm, above which it is considered “rain”. We have included both liquid mass partitions to facilitate comparisons with the two bulk cloud water and rain masses. However, these partitions are not included when examining process rates as processes rarely utilize this delimiter.

The naming of the process rates in Figure 4 uses the following conventions: Q refers to mixing ratio. The next two letters describe the microphysical process: (FZ: freezing, ML: melting, CD: condensation, EV: evaporation, CL: collection [or collision in HU-SBM], VD: vapor deposition, VS: vapor sublimation, CN: conversion, SH: shedding). The next two letters generally denote the sink and source mass categories, respectively (V: vapor, L: liquid, W: cloud water, R:

rain, C: column, P: plate, D: dendrite, I: cloud ice, S: snow, G: graupel, and H: hail). HU-SBM collisions have the next two letters after CL as the input colliding particles, while the final (or final two) letter(s) are source mass categories from the collision. For liquid, QFZLL and QMLLL denote total freezing and melting liquid mass changes, respectively. In the NSSL simulation, QFZRR and QCLIRR similarly denote total freezing, and rain and ice freezing rain mass changes, respectively. QCLRIG denotes rain and ice freezing to graupel. In the Thompson simulation, QCLGRR denotes possible rain source/sinks for graupel collecting rain, or vice versa depending on ambient temperature. QCLGGR is similar to QCLGRR, but for graupel mass. Finally, QCLRIG denotes rain and ice freezing to graupel, while QCLIRR represents rainwater sink from rain and ice freezing.

Cloud water mass is similar in the three simulations over the model run (Figures 3a-c). Condensation of liquid/cloud water dominates sources for these categories (Figures 4a,c,e). Cloud water itself likely does not contribute much to accumulated precipitation, but subsequent evolution (e.g., rain collection, riming) can modify it. Rainwater mass is much larger in the bulk simulations, with rainwater mass near 1.5 x 10^{-5} kg m^{-3} by the end of model runs compared to HU-SBM rainwater mass exceeding 0.75 x 10^{-5} kg m^{-3}. A reduction in rainwater mass relative to those in the two bulk simulations is consistent with smaller precipitation in the HU-SBM simulation. The largest liquid sinks in HU-SBM are either freezing, graupel riming, or collisions with ice particles to form graupel. The largest rain sources in both the NSSL (Figure 4i) and Thompson (Figure 4k) simulations are rain collecting cloud water and melting graupel, and larger than HU-SBM liquid sources (not including presumably cloud water condensation; Figure 4a). The Thompson simulation produces more rain than the NSSL simulation over the model run, in agreement with NSSL rain sinks (e.g., wet growth, freezing) exceeding those in Thompson rain (e.g., freezing, cloud ice-rain freezing). Still, the NSSL simulation precipitates more mass to the surface, which motivates our later examination of vertical hydrometeor and flux profiles.

The amount of cloud ice mass in HU-SBM, which is a sum of its column, plate, and dendrite mass, exceeds NSSL and Thompson simulated cloud ice mass (Figures 3d-f). This is entirely due to the large amount of liquid freezing to plates in the HU-SBM (Figures 4g,m,r). The NSSL and Thompson schemes also freeze liquid (i.e., cloud water) into cloud ice (Figures 4o,q), although not as much as the HU-SBM. The small amount of cloud ice in the Thompson simulation is consistent with prior studies: the scheme is known to aggressively convert cloud ice to snow (e.g, Van Weverberg et al., 2013) per the scheme's design (Figure 4q). Column mass exceeds dendrite mass in HU-SBM likely because of its larger nucleation temperature range. Snow mass is similar between the HU-SBM and Thompson simulations, which exceed that in the NSSL simulation. Snow aggregates in HU-SBM form by particle collisions; the large amount of HU-SBM plates provides a collisional source for aggregates, whether with themselves, other cloud ice particles, or aggregates (Figure 4b). The primary source of NSSL snow is freezing rain (Figure 4d), which provides a larger source for graupel than snow.

Rimed ice mass is typically largest in HU-SBM, as its simulated graupel mass is nearly 2 times larger than the NSSL and Thompson's graupel mass by the end of the model run (HU-SBM graupel ~7 x 10^{-5} kg m^{-3} vs. NSSL and Thompson graupel ~3.5-4 x 10^{-5} kg m^{-3}; Figures 3d-f). Much of HU-SBM's graupel comes from cloud ice freezing with liquid to graupel, and primarily grows by riming (Figure 4h). The largest graupel creation source in bulk simulations is freezing rain (although rain and ice freezing to graupel is prominent in the Thompson simulation; Figures 4j,l), and grow by wet growth. The bulk simulations have similar graupel mass source magnitudes but larger graupel sinks (i.e., melting) at the end of the model run compared to HU-SBM, explaining its larger graupel mass. This also implies graupel production and wet growth is likely not a major deficit of the HU-SBM. Thompson graupel mass is typically larger than NSSL graupel mass over the model run, except at the end. While this might be related to the large amount of rain freezing in the Thompson simulation and larger NSSL graupel sinks, Figure 4 does not include graupel sinks from sedimentation. HU-SBM hail mass is larger than that in NSSL at the end of the model run (HU-SBM hail ~1 x 10^{-5} kg m^{-3} vs NSSL hail ~0.5 x 10^{-5} kg m^{-3}). NSSL hail has larger sources (wet growth; Figure 4p) than HU-SBM hail (graupel and liquid freezing to hail, wet growth; Figure 4n), but also larger sinks (melting and shedding vs HU-SBM melting). More HU-SBM rimed ice does not lead to a larger rainwater mass field (i.e., melting) or accumulated precipitation. Again, we note that downdrafts are typically stronger in the bulk simulations than in HU-SBM. This motivates a further investigation into vertical distributions of hydrometeors, hydrometeor fluxes, and bin/bulk PSD assumptions to determine their effects on precipitation, which will be performed later.

3.2 Vertical profiles of hydrometeors and process rates

Vertical profiles of HWC are taken at a mature supercell stage (t = 100 min; Figure 1) to show their vertical distributions at this time (Figure 5). At each height level, the horizontal average of water content is calculated over the domain where condensate mixing ratio exceeds 0.01 g kg^{-1} to create vertical profiles. While HU-SBM simulates similar cloud water content over the duration of the storm, the vertical profile of its cloud water content is smaller compared to the NSSL and Thompson simulations (Figures 5a-c). However, its condensate coverage is larger than those of the NSSL and Thompson simulations (not shown). The NSSL produces more cloud water than the Thompson scheme at t =100 min (Figures 3b,c), also reflected in its vertical distribution. Cloud water content peaks near z = ~2-4 km in the each simulation. Cloud water content is dictated by the condensation rate (Figures 6a,c,e). In the bulk simulations, cloud water is depleted near z = 2-4 km by evaporation, rain collection, and autoconversion, while liquid in HU-SBM is generally depleted by evaporation.

Rainwater content is much smaller in HU-SBM compared to those in NSSL and Thompson, which is also the case with domain-averaged masses. Rainwater content in Thompson is generally larger than that in NSSL, similar to domain-averaged masses. Both bulk simulations have their rainwater content peaks near the surface, while HU-SBM rainwater peaks near z = ~3 km. HU-SBM rain sources near this peak are presumably melting ice (both rimed ice and snow aggregates), but might include condensation as well. There are little HU-SBM sinks near this height. Rain sources in the BMP simulations (which are larger) are melting rimed ice and collection of cloud water (while Thompson includes rain collecting graupel). These processes peak above the surface, especially cloud water collection. Therefore, the heights of rain peaks in BMP simulations seem to be more related to sedimentation and storm downdrafts, which will be discussed later. We also note here that low-level rain evaporation rates among the simulations are consistent with cold pool intensities in Figure 1 (i.e., Thompson rain evaporation is largest).

HU-SBM cloud ice water content peaks between z = 11-12 km, primarily from plate ice mass (Figure 5d). This height is similar to that of the peak level of NSSL cloud ice (z = ~12 km; Figure 5e), while Thompson ice peaks between z = 9-10 km. HU-SBM and NSSL cloud ice are primarily created through freezing liquid (Figures 6m,o). The lower Thompson cloud ice peak is the result of its aggressive conversion of cloud ice to snow, especially above 10 km (Figure 6q). Melting cloud ice does not significantly contribute to liquid in any of the microphyics simulations, which indicates its contribution to precipitation would likely manifest from conversion to other hydrometeors (e.g., conversion to snow and subsequently melting to rain, 3-component freezing to graupel, etc.). Still, snow only noticeably makes it to the melting level in HU-SBM, as its vertical profiles is near 0 kg m^{-3} in the NSSL and Thompson simulations. HU-SBM snow from snow-graupel collisions is larger than snow sources in BMP simulations near z = ~5 km (Figures 6b,d,f), in addition to crystal and snow collisions above.

Graupel vertical profiles are noticeably different across the three simulations: graupel water content peaks near z = 10 km in HU-SBM, while those in NSSL and Thompson simulations peak near z = 6 km and z = 5 km, respectively. While freezing rain provides similar graupel sources near z = 8 km for the bulk simulations, the Thompson scheme also contains a peak in cloud ice and rain freezing to graupel near z = 5 km (Figures 6j,l). HU-SBM graupel is primarily created through crystal-liquid collisions below z = 10 km (Figure 6h). While the HU-SBM graupel HWC peak is larger than those in NSSL and Thompson, it is not reflective of the large amount of graupel simulated over the duration of the simulated storm (Figure 3). Again, HU-SBM condensate coverage is larger than those in the bulk schemes (not shown). The weak downward graupel flux in HU-SBM inferred from its vertical profile hinders precipitation reaching the ground, as melting rimed ice is the primary source for low-level rain in these supercell simulations. HU-SBM hail water content peaks near z = 7 km, while NSSL hail peaks near z = 6 km and is able to reach the surface. HU-SBM hail is primarily created from graupel-liquid collisions near z = 6 km (Figure 6n). NSSL hail forms mostly from graupel conversion (Figure 4), and experiences more wet growth than HU-SBM hail (Figures 6n,p), allowing for greater hail growth potential despite its large shedding. HU-SBM hail melting occurs faster than NSSL hail in the melting layer, suggesting either larger NSSL hail size and/or greater NSSL downward hail transport.

4. Hydrometeor sedimentation and vertical fluxes

4.1 Fall speed parameterizations in different schemes

Vertical transport of hydrometeors at a mature supercell stage (t = 100 min) is further investigated to elaborate on the roles of storm kinematics, parameterized fall speed, PSD parameterizations, and underlying MP hydrometeor production with regard to precipitation near the surface. Updraft/downdraft HWC flux (defined here as $\rho w q_x$), hydrometeor sedimentation (defined as $-\rho v_t q_x$), and the net vertical hydrometeor flux ($\rho(w-v_t)q_x$) are utilized to analyze these roles, where ρ is ambient air density, q_x is the mixing ratio of hydrometeor x (e.g., rain), w is vertical velocity of the updraft/downdraft, and v_t is mass-weighted mean terminal velocity calculated from each scheme's fall speed parameterization. All fluxes are averaged at each vertical level over the horizontal domain where condensate mixing ratio exceeds 0.01 g kg^{-1} (Figure 7). Cloud water and ice are not included given their generally small fall speed.

NSSL rain sedimentation flux generally has larger magnitude than that of the Thompson below z = ~7 km (Figure 7a). While neither scheme's HWC is definitely larger over this depth (Figures 5b,c) and their rain fallspeed relationships are similar (Figure 8a), NSSL maximum rain v_t is larger than that of Thompson below z = ~8 km (not shown). Both bulk rain sedimentation fluxes have larger magnitude than that in HU-SBM, a consequence of the HU-SBM's comparatively small rainwater content. As Thompson snow fallspeed is slightly larger for melted particle diameter < ~2.5 mm (Figure 8a), generally larger Thompson snow mass results in larger snow sedimentation flux above z = 7-8 km, below which the larger HU-SBM snow mass results in greater sedimentation flux (Figure 7a). Downdrafts (negative w) containing rain and snow (Figure 7c) contribute to downward net snow flux near and above the melting level and net rain fluxes near the surface (Figure 7e). Downward net snow flux in the HU-SBM is larger than those in the bulk simulations near the melting level, but likely does not contribute directly to precipitation given its small magnitude. HU-SBM rain has smaller downward net flux near the surface compared to the two bulk simulations, partially due to weaker downdrafts. The NSSL simulation's largest downward net rain flux near the surface helps explain the scheme's largest accumulated precipitation (Figure 2).

HU-SBM rimed ice sedimentation flux is smaller than those of the bulk simulations (Figure 7b), even though its graupel and hail HWC peaks in the vertical profiles are largest. Its rimed ice fall speeds are smaller than those in NSSL (for equal constant density; not shown), and its graupel fall speed is progressively smaller than Thompson graupel for melted particle size > ~1.5 mm (Figure 8b), slowing its downward rimed ice transport. While upward rimed ice fluxes are large (Figure 7d), large sedimentation fluxes in bulk simulations result in overwhelmingly downward net rimed ice fluxes (Figure 7f). HU-SBM net graupel flux is upward between z = 6-11 km, a result of its slower fall speeds compared to the NSSL and Thompson schemes. Although Thompson graupel fall speed is smaller than that of NSSL graupel up to ice particle size of ~15 mm (for equal constant density; not shown), its larger graupel HWC (and typically larger downward transport in stronger downdrafts compared to HU-SBM and NSSL) provides a generally greater net flux below the melting level. HU-SBM hail also has a weaker downward net flux compared to NSSL hail, due to faster NSSL hail fall speeds (Figure 8b) and stronger downdrafts. Rimed ice contribution to precipitation can also be demonstrated below z = ~4 km, where the net rimed ice flux of each simulation decreases due to melting (although bulk net fluxes are larger).

4.2 Hydrometeor flux sensitivities to terminal velocity and PSD parameterization

The vertical fluxes of hydrometeors are further analyzed by examining their sensitivity to terminal velocity and bin/bulk PSD parameterization. This is performed in an offline mode, using hydrometeor model fields simulated by the original simulations at a mature stage (t = 100 min). To calculate the mass-weighted mean terminal velocities v_t using a bulk scheme formulation from the bin scheme-predicted hydrometeors, the bulk fall speed formulations are employed and the bulk PSDs are diagnosed using total bulk mass mixing ratios and number concentrations that were summed over the HU-SBM bins. To calculate v_t using the HU-SBM's formulations for the NSSL and Thompson schemes, the bulk hydrometeor species are discretized onto 33 mass bins based on their assumed PSDs (from their bulk mass and number concentrations), then use the HU-SBM fall speed formulations. The vertical velocities from the original simulations are used for vertical hydrometeor transport by updrafts/downdrafts.

Calculating the rain sedimentation flux using NSSL and Thompson fall speed formulations and treating HU-SBM rain as bulk rainwater increases the sedimentation flux relative to the flux using the native formulation (Figure 9a). In the bulk framework, HU-SBM rain now effectively has a smooth PSD across all diameters and is rid of its maximum mass limitation. Both bulk schemes assume an exponential distribution of rain with very similar fall speeds (Figure 8a), highlighting the effects of PSD parameterization on rain flux. Increasing HU-SBM rain sedimentation flux also increases its downward net flux toward the surface and reduces its upward flux (Figure 9c). The HU-SBM sedimentation and net rain fluxes calculated from NSSL and Thompson fall speeds and bulk PSD assumptions are still smaller in magnitude than NSSL and Thompson sedimentation and net rain fluxes near the surface. This is related to the underlying HU-SBM rain mass field dictated by HU-SBM liquid processes (i.e., melting ice particles), resulting in a smaller rain HWC vertical profile compared to the bulk simulations (Figures 5a-c). The HU-SBM snow sedimentation flux is generally unchanged near the melting level using NSSL and Thompson bulk formulations. Although NSSL and Thompson snow fall speeds can be faster than

HU-SBM snow fall speeds, constraining HU-SBM to a fixed PSD shape has the potential to introduce more small snow particles. As a result, HU-SBM net snow flux is also similar near the melting level when using NSSL and Thompson bulk formulations.

Replacing HU-SBM graupel and hail bins and fall speeds with NSSL fall speeds and bulk PSD assumptions (from HU-SBM q and N_t) significantly increases each category's sedimentation flux (Figure 9b). Rimed ice fall speed in the NSSL scheme exceeds that of HU-SBM (for equal constant density; not shown), increasing its downward transport. Using Thompson bulk graupel assumptions also increases HU-SBM graupel's sedimentation flux, although not as much as in NSSL. Thompson graupel fall speed is typically smaller than that of NSSL (Figure 8b). Increasing rimed ice sedimentation expectedly increases its downward net flux (Figure 9d), although the HU-SBM's underlying rimed ice production within the simulation precludes net flux increases near the surface relative to NSSL hail and Thompson graupel. Therefore, while increasing fall speeds in the HU-SBM scheme would increase surface precipitation, precipitation differences across the three microphysics schemes cannot be attributed to fall speed alone.

NSSL and Thompson rain and snow sedimentation fluxes subtly change when NSSL and Thompson bulk PSDs are discretized to the HU-SBM 33 mass bins and the fall speed formulations of HU-SBM are used at each bin (Figure 10a). The rain sedimentation fluxes near the surface are slightly reduced in the two bulk simulations. Rain fall speed relationships are similar among the three schemes (although HU-SBM liquid fall speed is slightly slower for drops < 1 mm; Figure 8a), while the HU-SBM mass bin discretization contains a maximum rain diameter of 6.5 mm, corresponding to very large raindrops. Thompson snow sedimentation flux is slightly reduced, likely attributed to generally slower HU-SBM fall speed. Therefore, Thompson net snow flux above the melting level and near-surface NSSL and Thompson net rain fluxes are slightly reduced (Figure 10c), but their near-surface net rain fluxes are larger than that in the HU-SBM simulation.

In contrast, the rimed ice sedimentation fluxes are reduced significantly for NSSL and Thompson but are still generally larger than those of HU-SBM rimed ice below z = ~9 km (Figure 10b). These reductions can be attributed to slower HU-SBM rimed ice fall speed relative to NSSL rimed ice fall speeds, and for melted particles larger than 1.5 mm relative to Thompson graupel fall speeds. Another contributing factor could be the HU-SBM maximum mass bins corresponding to NSSL and Thompson graupel size (at ρ_g = 500 kg m^{-3}) equal to 8.19 mm and NSSL hail size (at ρ_h = 900 kg m^{-3}) equal to 6.73 mm, reducing calculated v_t due to the truncated PSDs. Again, NSSL rimed ice density is predicted. The resulting increase in upward net flux and decrease in downward net flux of rimed ice to the melting level (Figure 10d) would reduce rimed ice melting to rain, and subsequently surface precipitation.

5. Summary and discussion

Idealized supercell simulations are performed in this study using the HU-SBM "full" spectral bin, and NSSL and Thompson bulk MP schemes available within WRF version 3.7.1. The HU-SBM simulation produces much less precipitation than the two bulk simulations over the 2 h simulations, and the behaviors of the schemes in the simulations are analyzed to investigate the main reasons for the precipitation differences. Domain-averaged and vertical profiles of process rates from the different simulations, as well as hydrometeor mass, water content, and vertical fluxes for different species are examined.

Over the two-hour duration of the simulated storm, the HU-SBM scheme simulates more cloud ice (plates), graupel, and hail, but less rainwater than the bulk simulations. HU-SBM appears to aggressively freeze large amounts of liquid to plate crystals, which can then aggregate to snow or freeze (along with other crystals) with liquid to graupel. Thompson simulates a large amount of snow mass similar to that in HU-SBM due to the scheme's aggressive cloud ice-snow conversion. Graupel in bulk simulations is primarily sourced from freezing rain, with additional contributions from cloud ice and rain freezing to graupel in the Thompson simulation. The larger HU-SBM graupel HWC peak above NSSL and Thompson graupel peaks in their vertical profiles (at a mature stage in simulations, t = 100 min) reflects its maximum mass bin limiting larger particles during 3-component freezing or wet growth. Smaller rimed ice particles combined with slower fall speeds leads to quicker updraft ejection. HU-SBM hail experiences less wet growth than NSSL hail, which may be due to or reflective of smaller updraft residency time.

The primary source of rain near the surface is from melting rimed ice, although HU-SBM additionally includes melting snow aggregates and the Thompson simulation includes rain collecting graupel. The lower HU-SBM rainwater amount near the surface is due to a greater contribution of slower-falling snow (itself sourced from ice crystal, snow, and graupel collisions) to rain compared to those in the bulk schemes, along with the previously-mentioned maximum mass bin limiting rimed ice particle size, and generally slower rimed ice fall speeds than those of the bulk schemes. Downward water mass transport is further complicated by HU-SBM's weakest downdrafts among the schemes, consistent with its smallest low-level evaporation rate.

In offline calculations for a single time (t = 100 min) at a mature stage of simulation, HU-SBM produces the smallest downward net rain flux to the surface because of its lowest rainwater content and weaker downdraft flux. This is likely due to a combination of net snow flux near the melting layer that is larger than those in the bulk simulations, and the smallest net graupel and hail fluxes at the melting level and surface. The smaller HU-SBM rimed ice net fluxes reflect generally slower rimed ice fall speeds and weaker downdraft fluxes. The NSSL simulation has a larger net rain flux to the surface than that in Thompson explaining its largest precipitation among the three simulations.

Downward net fluxes of rain and rimed ice for HU-SBM are increased when they are calculated using fall speed formulations of the NSSL and Thompson bulk schemes. When doing so, the discretized PSDs of HU-SBM are replaced with bulk PSDs (e.g., exponential or gamma distributions) by summing over the spectral bins to calculate q and N_t. Net rain fluxes near the surface are still smaller than those in bulk simulations, while net rimed ice fluxes near the surface are smaller than NSSL hail and Thompson graupel net fluxes. This can be attributed to the underlying smaller amounts of q_r, q_g, and q_h as seen in their vertical profiles. Conversely, discretizing the moment-based bulk PSDs in the NSSL and Thomspon schemes and calculating the fall speeds for the discretized bins using HU-SBM fall speed formulations slightly reduces near-surface downward net rain fluxes (due to slightly smaller HU-SBM fall speed and a maximum rain mass bin limiter). The downward net flux of rimed ice to the melting layer is also reduced, owing to the restrictive maximum rimed ice mass bins employed and typically smaller rimed ice fall speeds in the HU-SBM scheme. Still, the higher rain and rimed ice contents simulated by the bulk simulations (aided by stronger downdrafts) allow their downward net fluxes to typically exceed those in HU-SBM to the melting layer and surface.

We have demonstrated that, in a supercell framework, precipitation differences between MP schemes are more complex than just differences in simulated rainwater content or hydrometeor fall speeds. Understanding the main causes of the differences requires detailed analyses to gain insight on hydrometeor conversions/growth, interactions with storm dynamics (i.e., cold pool and updrafts/downdrafts), and subsequent vertical transport of hydrometeors. An important consideration for SBMs is the number of hydrometeor mass bins to allow for sufficient rimed ice growth within the scheme, especially for intense deep convection. Supercell storms tend to produce a large amount of rimed ice particles that contribute significantly to precipitation production. Adequate rimed ice wet growth facilitated by fast rimed ice fall speeds can ensure greater ice mass flux to the melting level and eventually to the surface after melting. Significant snow contribution to precipitation in supercells may be problematic and may require particle evolution adjustment (such as enhancing riming/wet growth given the large amount of plates from freezing liquid by HU-SBM that generally aggregate to snow, reducing snow-graupel collisions that convert graupel to snow), as snow particles sediment much slower than rimed ice. More rain in the melting layer sourced from rimed ice may provide dynamic feedback by strengthening downdrafts through evaporation, resulting in more negatively-buoyant air. Such insights are valuable to NWP researchers for model tuning, given the complexity of MP schemes from hydrometeor creation to surface precipitation. Comparisons of real-case supercell simulations to observations may further refine supercellular process representations and parameterizations by comparing the simulation with available observations. This is a subject for future work.

Acknowledgments

This research was primarily supported by the NOAA Warn-on-Forecast (WoF) grant by NA16OAR4320115. We thank two anonymous reviewers whose feedback improved the quality of this manuscript.

References

Bailey, M. P. and J. Hallett, 2009: A comprehensive habit diagram for atmospheric ice crystals: Confirmation from the laboratory, AIRS II, and other field studies. *J. Atmos. Sci.*, **66,** 2888–2899.

Benjamin, S. G., J. M. Brown, and T. G. Smirnova, 2016: Explicit precipitation-type diagnosis from a model using a mixed-phase bulk cloud–precipitation microphysics parameterization. *Wea. Forecasting*, **31,** 609–619.

Chen, S.-H. and W.-Y. Sun, 2002: A one-dimensional time dependent cloud model. *J. Meteor. Soc. Japan*, **80,** 99–118.

Cox, G. P., 1988: Modelling precipitation in frontal rainbands. *Quart J. Roy. Met. Soc.*, **114,** 115–127.

Dawson, D. T., E. R. Mansell, Y. Jung, L. J. Wicker, M. R. Kumjian, and M. Xue, 2014: Low-level ZDR signatures in supercell forward flanks: The role of size sorting and melting of hail. *J. Atmos. Sci.*, **71,** 276–299.

Falk, N. M., A. L. Igel, and M. R. Igel, 2019: The relative impact of ice fall speeds and microphysics parameterization complexity on supercell evolution. *Mon. Wea. Rev.*, **147,** 2403–2415.

Fan, J., and Coauthors, 2017: Cloud-resolving model intercomparison of an MC3E squall line case: Part I—Convective updrafts. *J. Geophy. Res.*, **122,** 9351–9378.

Ferrier, B. S., 1994: A double-moment multiple-phase four-class bulk ice scheme. Part I: Description. *J. Atmos. Sci.*, **51,** 249–280.

Field, P. R., R. J. Hogan, P. R. A. Brown, A. J. Illingworth, T. W. Choularton, and R. J. Cotton, 2005: Parametrization of ice-particle size distributions for mid-latitude stratiform cloud. *Q. J. R. Meteorol. Soc.*, **131,** 1997–2017.

Geresdi, I., 1998: Idealized simulation of the Colorado hailstorm case: Comparison of bulk and detailed microphysics. *Atmos. Res.*, **45,** 237–252.

Hall, W. D., 1980: A detailed microphysical model within a two-dimensional dynamic framework: Model description and preliminary results. *J. Atmos. Sci.*, **37,** 2486–2507.

Heikenfeld, M., B. White, L. Labbouz, and P. Stier, 2019: Aerosol effects on deep convection: the propagation of aerosol perturbations through convective cloud microphysics. *Atmos. Chem. Phys.*, **19,** 2601–2627.

Heymsfield, A. J. and M. Kajikawa, 1987: An improved approach to calculating terminal velocities of plate-like crystals and graupel. *J. Atmos . Sci.*, **44,** 1088–1099.

Hong, S.-Y., J. Dudhia, and S.-H. Chen, 2004: A revised approach to ice microphysical processes for the bulk parameterization of clouds and precipitation. *Mon. Wea. Rev.*, **132,** 103–120.

Jensen, A. A., J. Y. Harrington, H. Morrison, and J. A. Milbrandt, 2017: Predicting ice shape evolution in a bulk microphysics model. *J. Atmos. Sci.*, **74,** 2081–2104.

Johnson, M., Y. Jung, D. T. Dawson II, and M. Xue, 2016: Comparison of simulated polarimetric signatures in idealized supercell storms using two-moment bulk microphysics schemes in WRF. *Mon. Wea. Rev.*, **144,** 971–996.

Johnson, M., Y. Jung, J. A. Milbrandt, H. Morrison, and M. Xue, 2019: Effects of the representation of rimed ice in bulk microphysics schemes on polarimetric signatures. *Mon. Wea. Rev.*, **147,** 3785–3810.

Jung, Y., G. Zhang, and M. Xue, 2008: Assimilation of simulated polarimetric radar data for a convective storm using the ensemble Kalman filter. Part I: Observation operators for reflectivity and polarimetric variables. *Mon. Wea. Rev.*, **136,** 2228–2245.

Khain, A. and B. Lynn, 2009: Simulation of a supercell storm in clean and dirty atmosphere using weather research and forecast model with spectral bin microphysics. *J. Geophy. Res.*, **114,** D19209.

Khain, A., B. Lynn, and J. Shpund, 2016: High resolution WRF simulations of Hurricane Irene: Sensitivity to aerosols and choice of microphysical schemes. *Atmos. Res.*, **167,** 129–145.

Khain, A., A. Pokrovsky, M. Pinsky, A. Seifert, and V. Phillips, 2004: Simulation of effects of atmospheric aerosols on deep turbulent convective clouds using a spectral microphysics mixed-phase cumulus cloud model. Part I: Model description and possible applications. *J. Atmos. Sci.*, **61,** 2963–2982.

Khain, A. P. and I. Sednev, 1996: Simulation of precipitation formation in the eastern Mediterranean coastal zone using a spectral microphysics cloud ensemble model. *Atmos. Res.*, **55,** 77–110.

Khain, A. P., and Coauthors, 2015: Representation of microphysical processes in cloud-resolving models: Spectral (bin) microphysics versus bulk parameterization. *Rev. Geophys.*, **53,** 247–322.

Kumjian, M. R. and A. V. Ryzhkov, 2008: Polarimetric signatures in supercell thunderstorms. *J. Appl. Meteor. Climatol.*, **47,** 1940–1961.

Kumjian, M. R., A. P. Khain, N. Benmoshe, E. Ilotoviz, A. V. Ryzhkov, and V. T. J. Phillips, 2014: The anatomy and physics of ZDR columns: Investigating a polarimetric radar signature with a spectral bin microphysical model. *J. Appl. Meteor. Climatol.*, **53,** 1820–1843.

Lin, Y.-L., R. D. Farley, and H. D. Orville, 1983: Bulk parameterization of the snow field in a cloud model. *J. Climate Appl. Meteor.*, **22,** 1065–1092.

Magono, C. and C. W. Lee, 1966: Meteorological classification of natural snow crystals. *J. Fac. Sci. Hokkaido Univ. Ser. 7*, **2,** 321–335.

Mansell, E. R., C. L. Ziegler, and E. C. Bruning, 2010: Simulated electrification of a small thunderstorm with two-moment bulk microphysics. *J. Atmos. Sci.*, **67,** 171–194.

Matrosov, S. Y., R. F. Reinking, R. A. Kropfli, and B. W. Bartram, 1996: Estimation of ice hydrometeor types and shapes from radar polarization measurements. *J. Atmos. Oceanic Technol.*, **13,** 85–96.

Milbrandt, J. A. and M. K. Yau, 2005a: A multimoment bulk microphysics parameterization. Part I: Analysis of the role of the spectral shape parameter. *J. Atmos. Sci.*, **62,** 3051–3064.

Milbrandt, J. A. and M. K. Yau, 2005b: A multimoment bulk microphysics parameterization. Part II: A proposed three-moment closure and scheme description. *J. Atmos. Sci.*, **62,** 3065–3081.

Milbrandt, J. A., H. Morrison, D. T. Dawson II, and M. Paukert, 2021: A triple-moment representation of ice in the predicted particle properties (P3) microphysics scheme. *J. Atmos. Sci.*, **78,** 439–458.

Mitchell, D. L., R. Zhang, and R. L. Pitter, 1990: Mass-dimensional relationships for ice particles and the influence of riming on snowfall rates. *Journal of Applied Meteorology*, **29,** 153–163.

Morrison, H. and J. A. Milbrandt, 2015: Parameterization of cloud microphysics based on the prediction of bulk ice particle properties. Part I: Scheme description and idealized tests. *J. Atmos. Sci.*, **72,** 287–311.

Morrison, H., G. Thompson, and V. Tatarskii, 2009: Impact of cloud microphysics on the development of trailing stratiform precipitation in a simulated squall line: Comparison of one- and two-moment schemes. *Mon. Wea. Rev.*, **137,** 991–1007.

Morrison, H., and Coauthors, 2020: Confronting the challenge of modeling cloud and precipitation microphysics. *Journal of Advances in Modeling Earth Systems*, **12,** e2019MS001689.

Pruppacher, H. R. and J. D. Klett, 1997: *Microphysics of clouds and precipitation*. 2nd ed. Kluwer Academic Publishers, 954 pp.

Reisin, T., Z. Levin, and S. Tzivion, 1996: Rain production in convective clouds as simulated in an axisymmetric model with detailed microphysics. Part I: Description of the model. *J. Atmos. Sci.*, **53,** 497–519.

Ryzhkov, A., M. Pinsky, A. Pokrovsky, and A. Khain, 2011: Polarimetric radar observation operator for a cloud model with spectral microphysics. *J. Appl. Meteor. Climatol.*, **50,** 873–894.

Shpund, J., and Coauthors, 2019: Simulating a mesoscale convective system using WRF with a new spectral bin microphysics: 1: Hail vs graupel. *J. Geophy. Res.: Atmos.*, **124,** 14072-14101.

Skamarock, W. C., and Coauthors, 2008: A description of the Advanced Research WRF version 3. NCAR Tech. Note NCAR/TN-475+STR, 125 pp.

Takahashi, T., 1976: Hail in an axisymmetric cloud model. *J. Atmos. Sci.*, **33,** 1579-1601.

Thompson, G., P. R. Field, R. M. Rasmussen, and W. D. Hall, 2008: Explicit forecasts of winter precipitation using an improved bulk microphysics scheme. Part II: Implementation of a new snow parameterization. *Mon. Wea. Rev.*, **136,** 5095–5115.

Ulbrich, C. W., 1983: Natural variations in the analytical form of the raindrop size distribution. *J. Appl Meteor. Climatol.*, **22,** 1764–1775.

Van Weverberg, K., and Coauthors, 2013: The role of cloud microphysics parameterization in the simulation of mesoscale convective system clouds and precipitation in the tropical western Pacific. *J. Atmos. Sci.*, **70,** 1104–1128.

Vivekanandan, J., W. M. Adams, and V. N. Bringi, 1991: Rigorous approach to polarimetric radar modeling of hydrometeor orientation distributions. *Journal of Applied Meteorology*, **30,** 1053–1063.

Waterman, P. C., 1969: Scattering by dielectric obstacles. *Alta Freq.*, **38,** 348–352.

Weisman, M. L. and J. B. Klemp, 1982: The dependence of numerically simulated convective storms on vertical wind shear and buoyancy. *Mon. Wea. Rev.*, **110,** 504–520.

Xue, L., and Coauthors, 2017: Idealized simulations of a squall line from the MC3E field campaign applying three bin microphysics schemes: dynamic and thermodynamic structure. *Mon. Wea. Rev.*, **145,** 4789–4812.

Young, K. C., 1974: A numerical simulation of wintertime, orographic precipitation. Part I: Description of model microphysics and numerical techniques. *J. Atmos. Sci.*, **31,** 1735–1748.

Zrnic, D. S., N. Balakrishnan, C. L. Ziegler, V. N. Bringi, K. Aydin, and T. Matejka, 1993: Polarimetric signatures in the stratiform region of a mesoscale convective system. *J. Appl. Meteor. Climatol.*, **32,** 678–693.

Figure Captions

Figure 1. Horizontal reflectivity (*ZH* [dBZ]; left column) through each storm's updraft and potential temperature perturbations Θ' (K; right column) near z = ~280 m for the (a,b) HU-SBM, (c,d) NSSL, and (e,f) Thompson microphysics schemes at t = 100 min. Blue lines in vertical cross sections denote the 0 °C isotherm, while black contours are vertical velocity which start at 10 m s-1 with a 15 m s-1 interval. Reflectivity contours (grey) are shown in Θ' subplots for 15, 30, and 45 dBZ, and the wind field is represented by vectors. Updraft contours at z = ~2 km are shown as magenta contours for w = 10 m s-1, while downdraft contours at z = ~2 km are shown as black contours for w = -10, -5, and -2 m s-1 in Θ' subplots. Vertical black lines in Θ' plots denote where vertical cross sections are taken.

Figure 2. Domain-averaged accumulated precipitation (mm) over the duration of the model run for the HU-SBM, NSSL, and Thompson microphysics schemes.

Figure 3. Time series of domain-averaged mass (kg m-3) for (top row) liquid and (bottom row) ice hydrometeors for the (a,d) HU-SBM, (b,e) NSSL, and (c,f) Thompson microphysics schemes over the duration of the model run.

Figure 4. Domain-averaged 5-min accumulated mixing ratio process rates (g kg-1) for the (left two columns) HU-SBM, (middle two columns) NSSL, and (right two columns) Thompson microphysics schemes. Plot labels indicate the relevant hydrometeor.

Figure 5. Vertical profiles of horizontally-averaged hydrometeor water content (kg m-3) for liquid (top row) and ice (bottom row) hydrometeors for the (a,d) HU-SBM, (b,e) NSSL, and (c,f) Thompson microphysics schemes at t = 100 min.

Figure 6. Vertical profiles of horizontally-averaged 5-min accumulated mixing ratio process rates (g kg^{-1}) for the (left two columns) HU-SBM, (middle two columns) NSSL, and (right two columns)

Thompson microphysics schemes at t = 100 min. Plot labels indicate the relevant hydrometeor. The vertical black line in each plot denotes zero.

Figure 7. Vertical profiles of horizontally-averaged hydrometeor water content fluxes (kg m^{-2} s^{-1}) calculated with (a,b) mass-weighted mean hydrometeor fall speed (v_t), (c,d) updraft/downdrafts (w), and (e,f) their net ($w - v_t$) vertical speed for (left column) rain and snow, and (right column) graupel and hail hydrometeors at t = 100 min. PSDs and fall speeds to calculate v_t are consistent with each microphysics scheme's parameterizations.

Figure 8. Terminal velocities (m s^{-1}) spaced at HU-SBM mass bins (but shown here relative to melted diameter (mm)) of (a) rain (or HU-SBM liquid) and snow, and (b) graupel and hail in the HU-SBM, NSSL, and Thompson schemes. The "_vx" suffix denotes the relationship for hydrometeor x. Terminal velocities are plotted in each microphysics' reference state (i.e., pressure = 1000 hPa in HU-SBM, air density ρ_a = 1.225 and 1.185 kg m^{-3} in the NSSL and Thompson schemes, respectively). NSSL graupel and hail fall speeds are displayed with bulk densities of ρ_g = 500 and ρ_h = 900 kg m^{-3}, respectively.

Figure 9. Vertical profiles of horizontally-averaged hydrometeor water content fluxes (kg m^{-2} s^{-1}) calculated with (a,b) mass-weighted mean hydrometeor fall speed (v_t), and (c,d) their net ($w - v_t$) vertical speed for (left column) rain and snow, and (right column) graupel and hail hydrometeors at t = 100 min. HU-SBM PSDs and fall speed parameterizations to calculate v_t follow original HU-SBM parameterizations (HU-SBM_x), or those in the NSSL (HU-SBM_nssl_x) or Thompson (HU-SBM_thom_x) schemes for hydrometeor x.

Figure 10. As in Figure 9, with NSSL and Thompson PSDs and fall speed parameterizations following those in the HU-SBM scheme.

Table 1. WRF model input.

WRF Model Configuration	
Run time	120 min
Δt	6 s
Sound wave Δt	1 s
Model output interval	10 min
Horizontal domain	200 km x 200 km
Model lid	20 km
Δx	1 km
Δy	1 km
Δz	~500 m
Time integration scheme	Third order Runge-Kutta
Horizontal momentum advection	Fifth order
Vertical momentum advection	Third order
Horizontal scalar advection	Fifth order
Vertical scalar advection	Third order
Upper level damping	5000 m below model top
Rayleigh damping coefficient	0.003
Turbulence	3-D 1.5 order turbulent kinetic energy (TKE) closure
Horizontal boundary conditions	Open

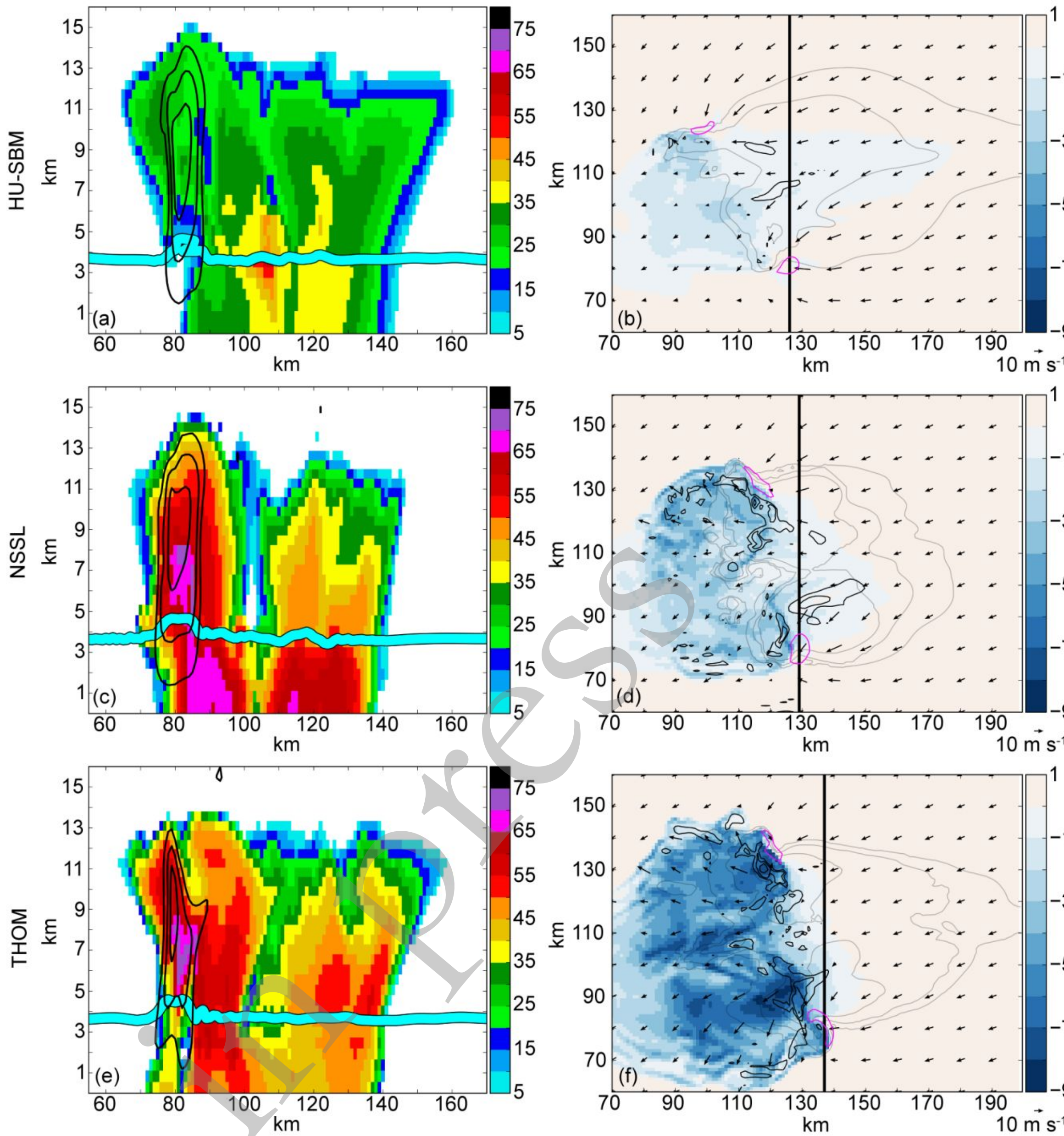

Figure 1. Horizontal reflectivity (Z_H [dBZ]; left column) through each storm's updraft and potential temperature perturbations Θ' (K; right column) near z = ~280 m for the (a,b) HU-SBM, (c,d) NSSL, and (e,f) Thompson microphysics schemes at t = 100 min. Blue lines in vertical cross sections denote the 0 °C isotherm, while black contours are vertical velocity which start at 10 m s^{-1} with a 15 m s^{-1} interval. Reflectivity contours (grey) are shown in Θ' subplots for 15, 30, and 45 dBZ, and the wind field is represented by vectors. Updraft contours at z = ~2 km are shown as magenta contours for w = 10 m s^{-1}, while downdraft contours at z = ~2 km are shown as black contours for w = -10, -5, and -2 m s^{-1} in Θ' subplots. Vertical black lines in Θ' plots denote where vertical cross sections are taken.

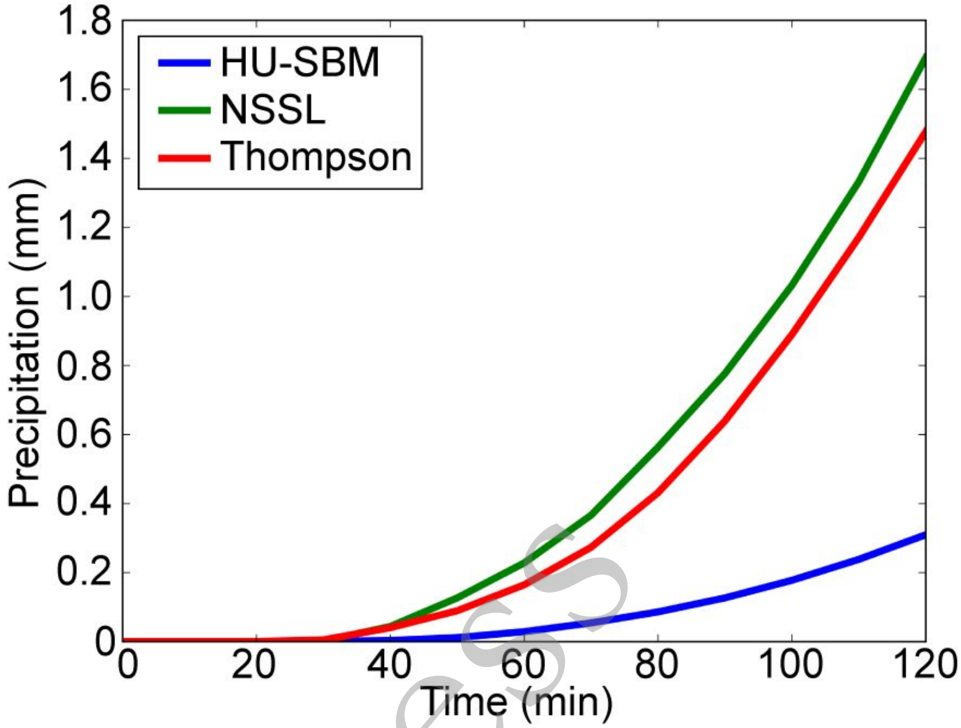

Figure 2. Domain-averaged accumulated precipitation (mm) over the duration of the model run for the HU-SBM, NSSL, and Thompson microphysics schemes.

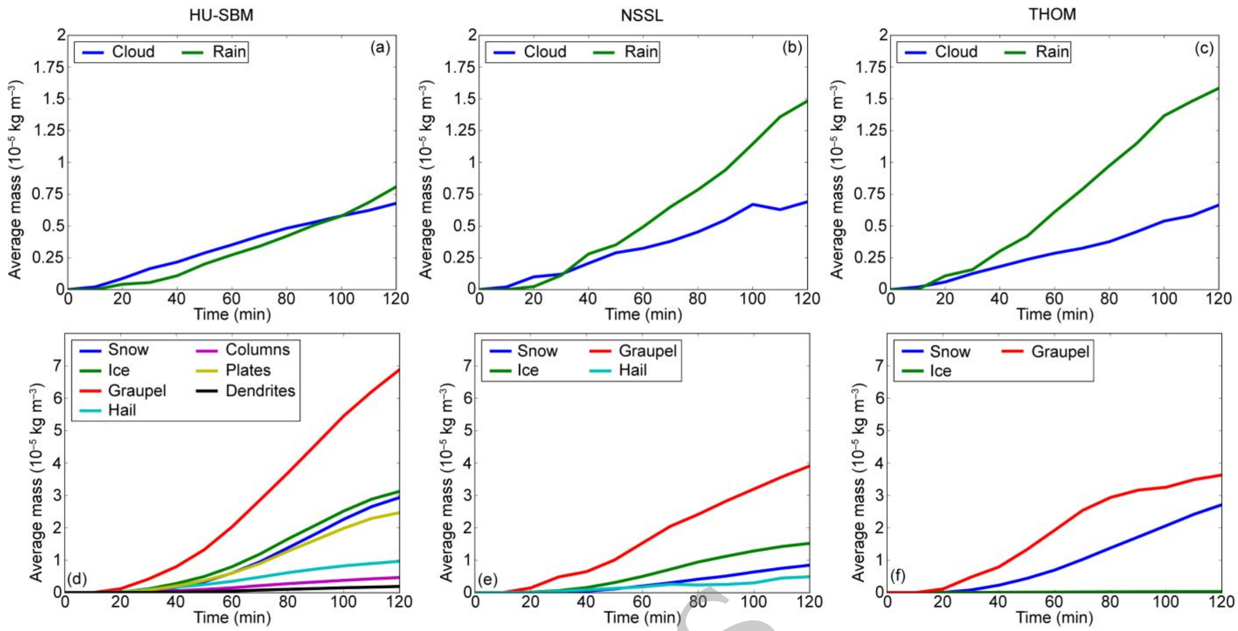

754 Figure 3. Time series of domain-averaged mass (kg m^{-3}) for (top row) liquid and (bottom row) ice hydrometeors for the (a,d) HU-
755 SBM, (b,e) NSSL, and (c,f) Thompson microphysics schemes over the duration of the model run.

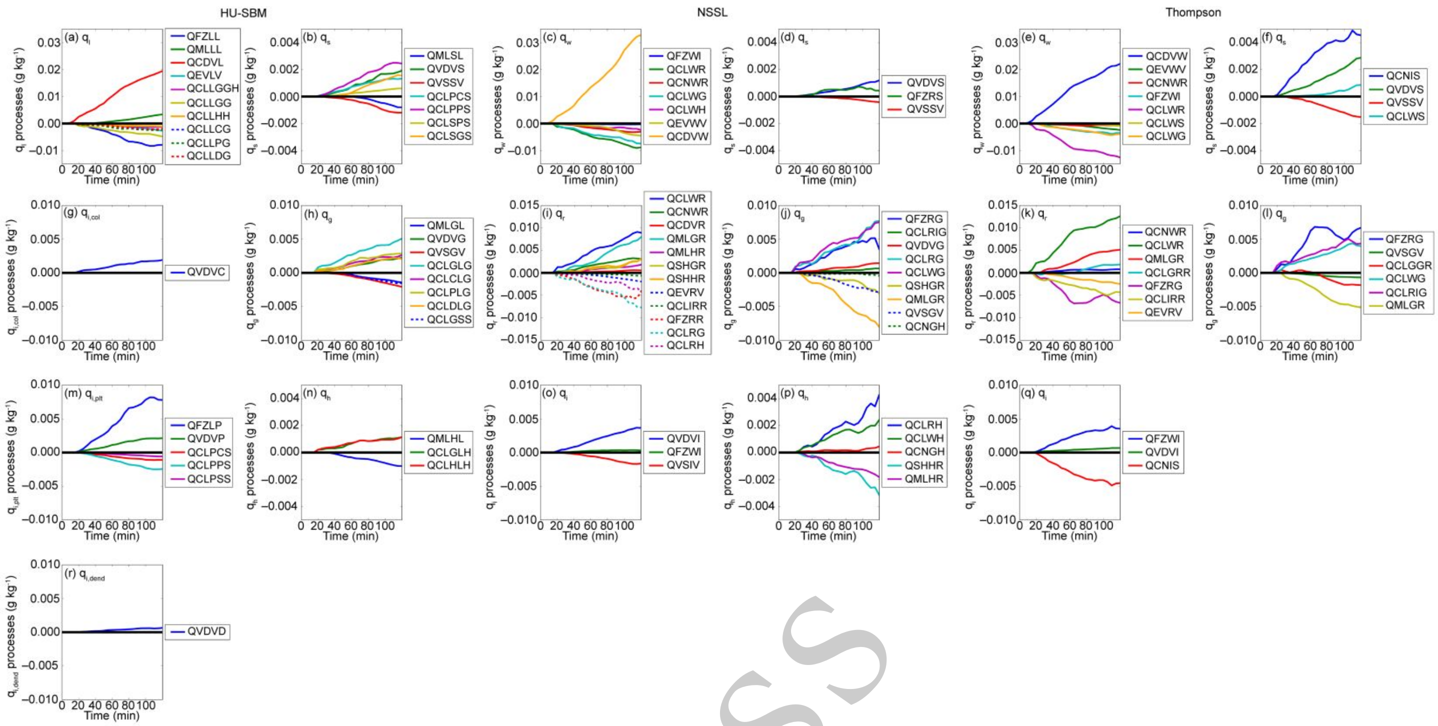

Figure 4. Domain-averaged 5-min accumulated mixing ratio process rates (g kg^{-1}) for the (left two columns) HU-SBM, (middle two columns) NSSL, and (right two columns) Thompson microphysics schemes. Plot labels indicate the relevant hydrometeor.

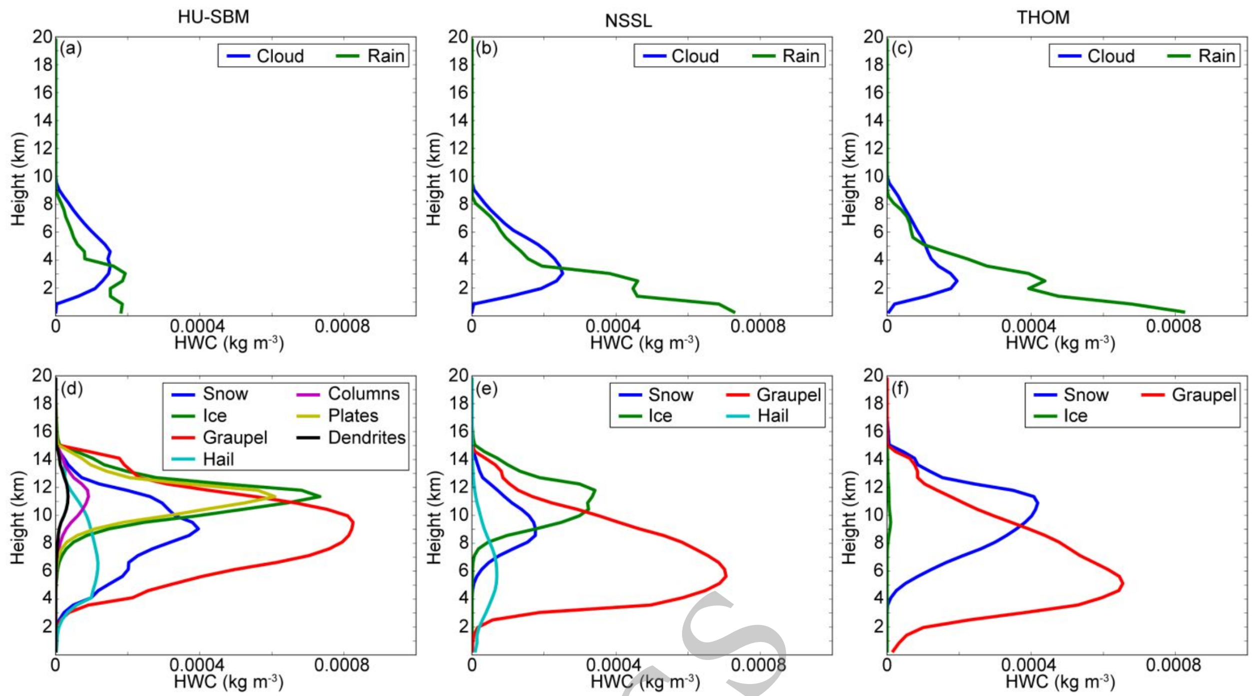

Figure 5. Vertical profiles of horizontally-averaged hydrometeor water content (kg m^{-3}) for liquid (top row) and ice (bottom row) hydrometeors for the (a,d) HU-SBM, (b,e) NSSL, and (c,f) Thompson microphysics schemes at t = 100 min.

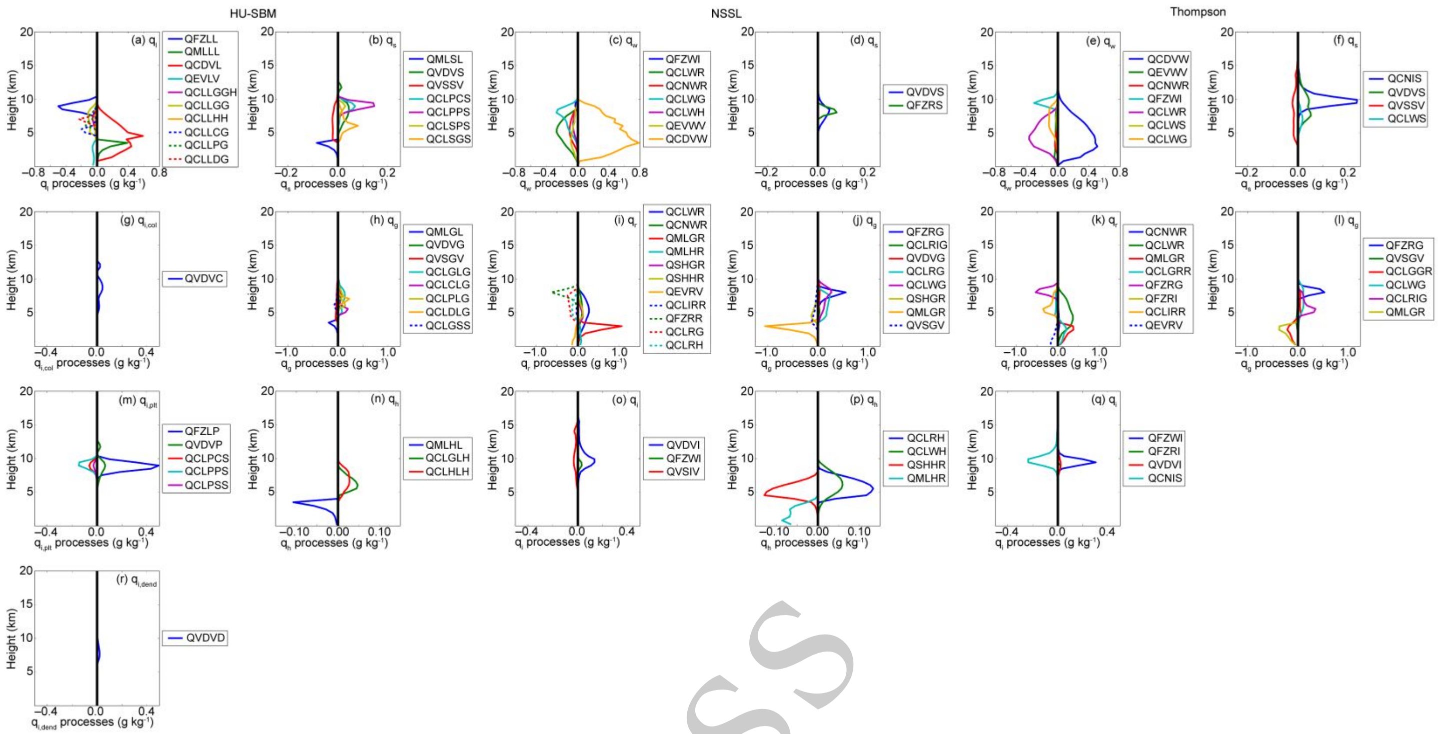

Figure 6. Vertical profiles of horizontally-averaged 5-min accumulated mixing ratio process rates (g kg^{-1}) for the (left two columns) HU-SBM, (middle two columns) NSSL, and (right two columns) Thompson microphysics schemes at t = 100 min. Plot labels indicate the relevant hydrometeor. The vertical black line in each plot denotes zero.

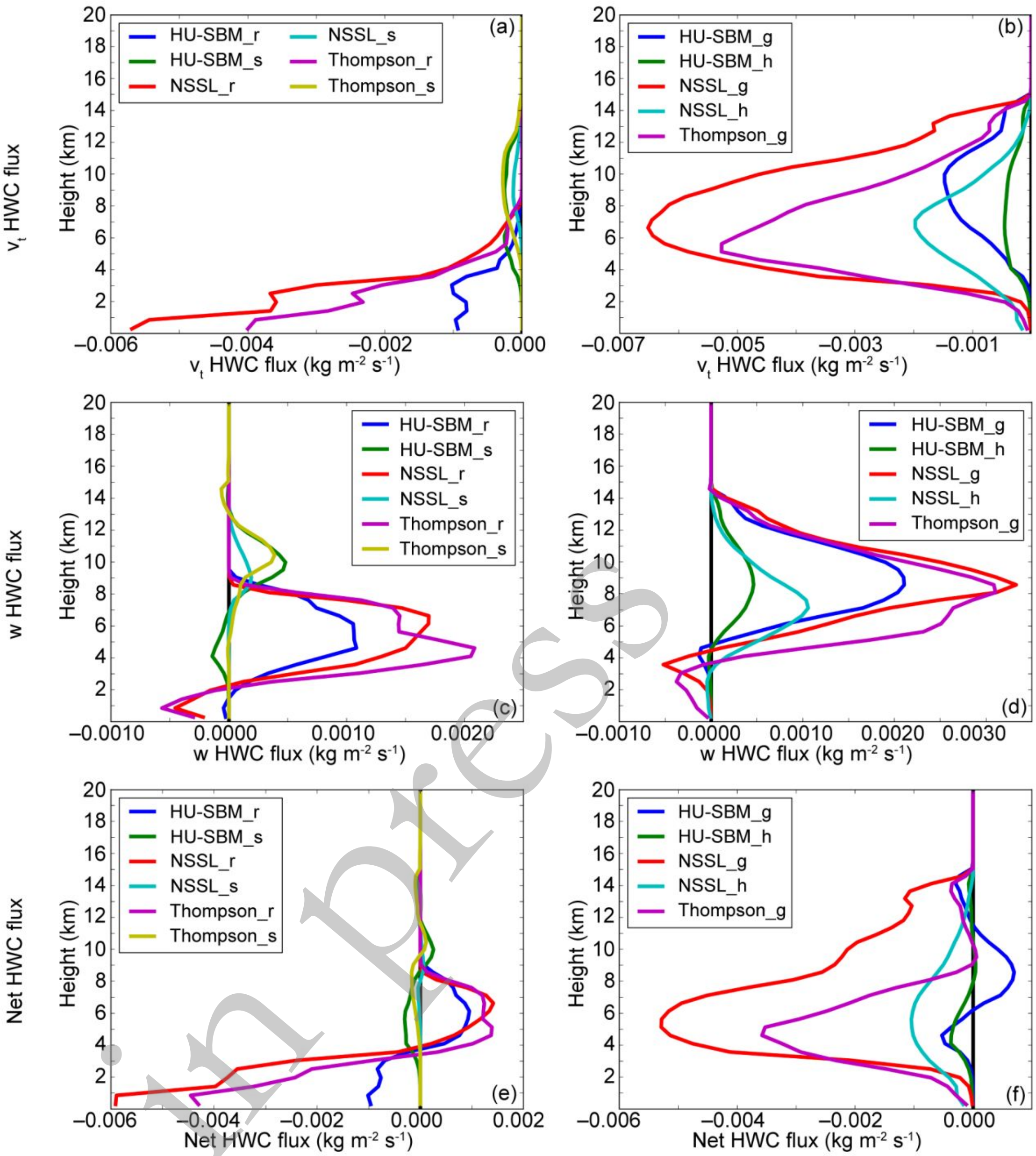

Figure 7. Vertical profiles of horizontally-averaged hydrometeor water content fluxes (kg m^{-2} s^{-1}) calculated with (a,b) mass-weighted mean hydrometeor fall speed (v_t), (c,d) updraft/downdrafts (w), and (e,f) their net ($w - v_t$) vertical speed for (left column) rain and snow, and (right column) graupel and hail hydrometeors at t = 100 min. PSDs and fall speeds to calculate v_t are consistent with each microphysics scheme's parameterizations.

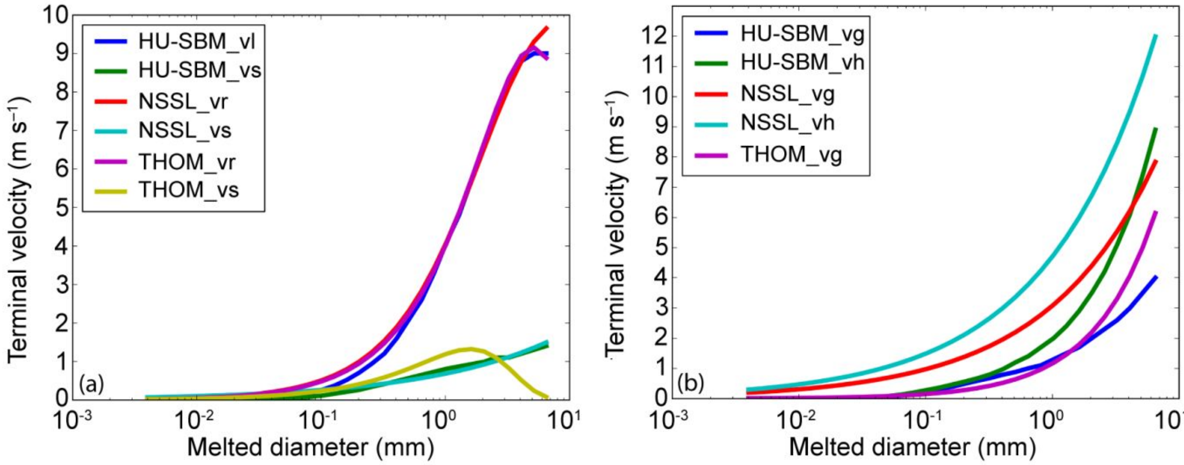

Figure 8. Terminal velocities (m s^{-1}) spaced at HU-SBM mass bins (but shown here relative to melted diameter (mm)) of (a) rain (or HU-SBM liquid) and snow, and (b) graupel and hail in the HU-SBM, NSSL, and Thompson schemes. The "_vx" suffix denotes the relationship for hydrometeor x. Terminal velocities are plotted in each microphysics' reference state (i.e., pressure = 1000 hPa in HU-SBM, air density ρ_a = 1.225 and 1.185 kg m^{-3} in the NSSL and Thompson schemes, respectively). NSSL graupel and hail fall speeds are displayed with bulk densities of ρ_g = 500 and ρ_h = 900 kg m^{-3}, respectively.

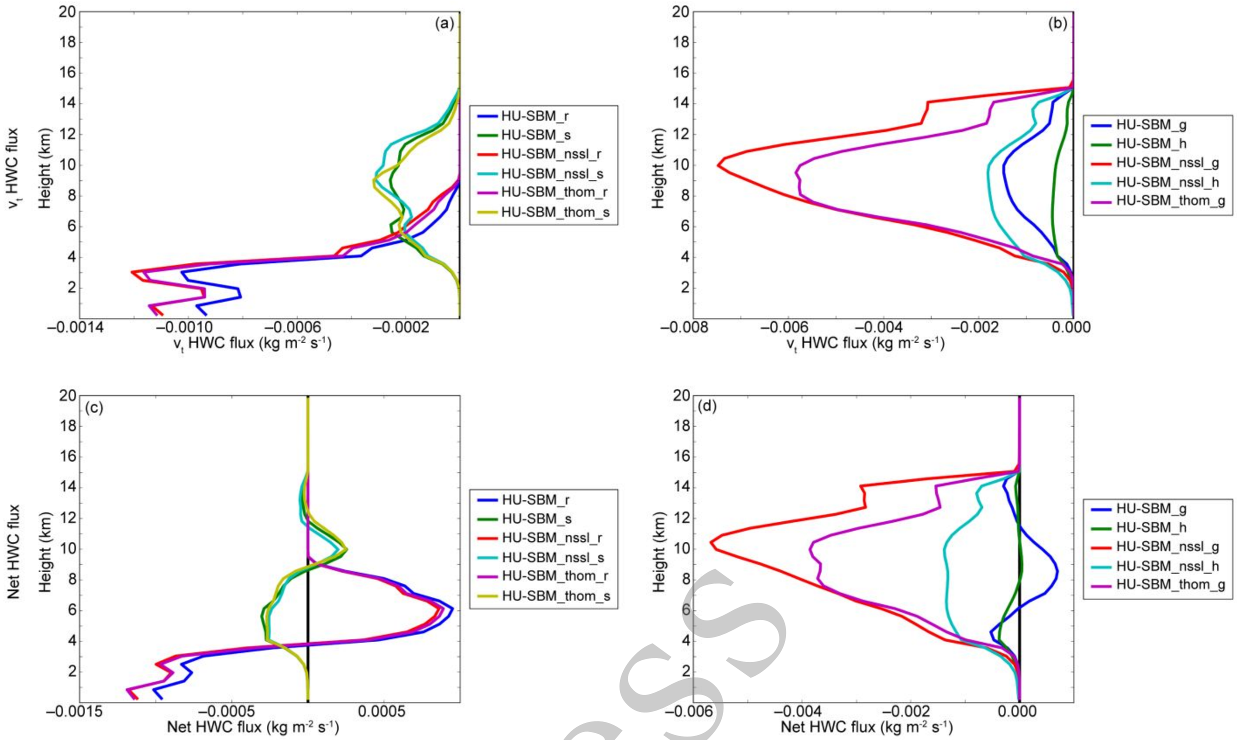

Figure 9. Vertical profiles of horizontally-averaged hydrometeor water content fluxes (kg m^{-2} s^{-1}) calculated with (a,b) mass-weighted mean hydrometeor fall speed (v_t), and (c,d) their net ($w - v_t$) vertical speed for (left column) rain and snow, and (right column) graupel and hail hydrometeors at t = 100 min. HU-SBM PSDs and fall speed parameterizations to calculate v_t follow original HU-SBM parameterizations (HU-SBM_x), or those in the NSSL (HU-SBM_nssl_x) or Thompson (HU-SBM_thom_x) schemes for hydrometeor x.

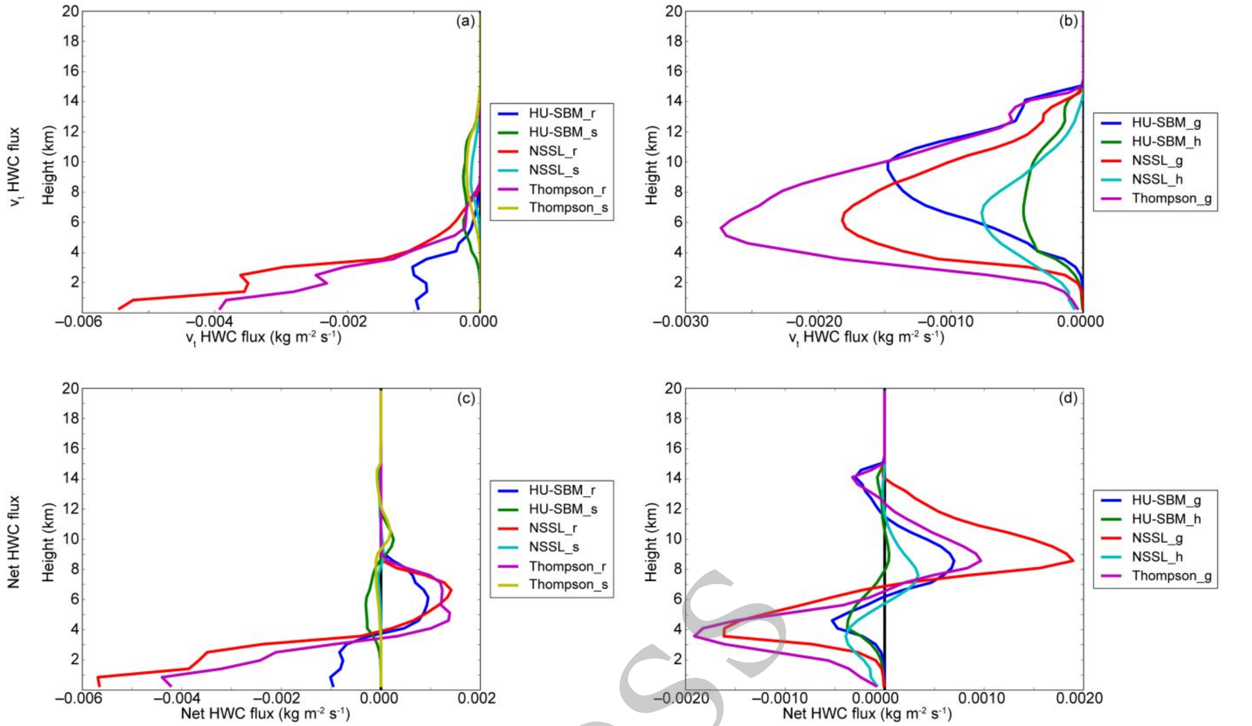

Figure 10. As in Figure 9, with NSSL and Thompson PSDs and fall speed parameterizations following those in the HU-SBM scheme.